Nanoplasmonic In Situ Spectroscopy for Catalysis Applications

Christoph Langhammer*[,†] and Elin M. Larsson[†,‡,§]

[†]Department of Applied Physics, [‡]Competence Center for Catalysis, Chalmers University of Technology, S-412 96 Göteborg, Sweden
[§]Insplorion AB, Stena Center 1C, S-412 92 Göteborg, Sweden

1. INTRODUCTION

In catalysis, reactants in gas or liquid phase are often converted to desired product molecules on the surface of catalytically active nanoparticles. Closing the gaps between fundamental research and applications in chemical industry or the energy-related areas is one of the major challenges in the field. The "pressure gap" originates from the need of most surface sensitive techniques to operate at low pressures or even in ultrahigh vacuum (UHV). This strongly contrasts "real" catalyzed reactions that are carried out at atmospheric pressure or up to several hundred bars. The "material gap" arises because of the fact that many experimental studies use simplified model systems such as single crystals that cannot represent the complex structure of a "real" catalyst.

Another significant challenge when studying catalyst nano-materials is unwanted "artifacts" and averaged responses due to inhomogeneous sample material. Such effects are always present in data obtained from catalyst particle ensembles or due to the lack of sensitivity or spatial resolution of the used probes (or both). The artifacts are mainly caused by heterogeneous size distributions, differences in the local chemistry and structure of nanoentities in the ensemble, and local temperature or mass-transport gradients in large sample volumes. Thus, they can hide crucial information linked to the individual characteristics of the studied objects.

Here, we highlight a new experimental approach with the potential to contribute significantly to bridging the material and pressure gaps due to its suitability to probe catalyst materials in situ and in operando. Furthermore, the concept facilitates probing of *single* functional nanoparticles and is thus expected to alleviate significantly the aforementioned detrimental inhomogeneous sample material related effects in catalysis science. As discussed in detail below, combination with other techniques such as electron microscopy in some cases and careful experimental design are a key ingredient if quantitative information is to be obtained.

The *optical* indirect nanoplasmonic sensing (INPS) concept was first presented in 2009[1,2] and utilizes the localized surface plasmon resonance (LSPR) excitation in gold sensor nano-particles at visible light frequencies to probe processes and changes on/in adjacent catalyst nanoparticles (and other nanomaterials) via the locally enhanced plasmonic near field (refractometric sensing) or through the intrinsic temperature sensitivity of the LSPR (optical nanocalorimetry). The utilized gold sensor nanoparticles feature a "nanodisk" geometry with a diameter on the order of 100 nm and a thickness of 20 nm, and they are covered by a typically 10-nm-thick dielectric spacer layer with a number of functions detailed below. The key features of INPS, which make it a very promising emerging in situ spectroscopy technique for catalysis applications, are (i) a surface-based sensor operating with small amounts of sample material (a few percents of a monolayer is enough for an ensemble measurement), (ii) high temporal resolution in the millisecond range (in principle, dictated by the minimal integration time offered by the CCD detector), (iii) compatibility with high temperatures (limitations discussed below) and pressure (atmospheric or higher) in a harsh chemical environment, (iv) compatibility with a wide range of support materials, and (v) the possibility to probe individual nanoparticles. These specific capabilities will be discussed by reviewing a number of recent studies in which INPS was successfully used.

2. LOCALIZED SURFACE PLASMON RESONANCE

The interaction of near-visible light with a metallic surface can excite resonant collective oscillations in the electronic system. If these oscillations are localized to a nanosized entity such as a metal nanoparticle, they are referred to as LSPRs or particle plasmons and can be understood as time-dependent oscillating electric dipoles (Figure 1a). Because of the resonant nature of the phenomenon, LSPR gives rise to a very strong interaction of light with the nanoparticle via light absorption and scattering.[3] Furthermore, the polarization of the electronic system creates locally strongly enhanced electromagnetic fields (with respect to the incoming field), as illustrated in Figure 1b and c. The figure comprises a cross section and top view, respectively, trough/onto a Au disk-like nanoparticle ("nano-disk") with a diameter of 80 nm and a thickness of 20 nm illuminated at the resonance wavelength. The color-coding illustrates schematically the locally enhanced dipolar field surrounding the particle, as calculated by the finite-difference time domain (FDTD) method. We specifically note that the enhanced field decays first exponentially and, at longer distances, in a basically linear manner from the surface of the plasmonic nanoparticle. In this way, a spatially nanoconfined *sensing volume*, extending a few tens of nanometers from the particle surface, is created. Within it, minute *local* changes can be detected if they involve a change of the polarizability of the matter localized within the sensing volume. Such changes, as shown below, may be the addition/removal of moieties, the rearrangement of material or another change, such as a phase transition, a solid-state reaction, or the presence of different types of adsorbate molecules. In a typical sensing application of plasmonic nanoparticles, they are thus used as transducers, which translate the local changes of interest into a slightly changed resonance condition for the LSPR, which in turn is reflected in a (often tiny) shift of the resonance wavelength.
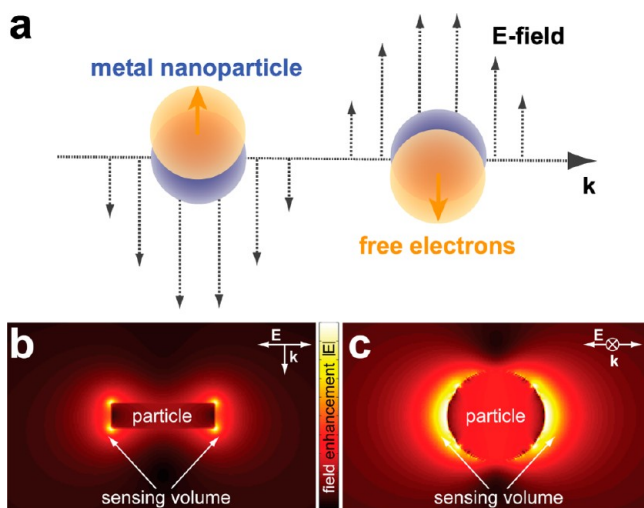
Figure 1. (a) Interaction of near-visible light with a nanosized metallic particle can excite resonant collective oscillations in the electronic system, which are referred to as localized surface plasmon resonances or particle plasmons. As sketched, these resonances can be understood as time-dependent oscillating electric dipoles. (b) Cross section and (c) top view trough/onto a Au nanodisk particle with a diameter of 80 nm and a thickness of 20 nm illuminated at the LSP resonance wavelength. The color-coding illustrates schematically the locally enhanced dipolar field surrounding the particle, as calculated by the finite-difference time domain method. The enhanced field region constitutes a spatially nanoconfined *sensing volume*, extending a few tens of nanometers from the particle surface, within which even tiny local polarizability changes can be detected. The plotted local field amplitudes |*E*| are normalized to the incident light.

The latter can then be read-off *remotely* with high resolution by means of rather simple optical transmission or reflection spectroscopy. This, in essence, makes plasmonic nanoparticles very efficient optical antennas that (i) are very sensitive to events occurring in their nanoenvironment and that (ii) can be very efficiently used to send information to or obtain information from the nanoworld by means of near-visible light. Furthermore, the intrinsic temperature sensitivity of the plasmon resonance makes it possible to use it as an efficient nanosized optical thermometer for calorimetry-type experiments.

3. A SHORT HISTORY OF NANOPLASMONIC SENSING

Plasmonic nanoparticles have been widely explored for biosensing applications since the end of the 1990s. The first report on surface-based LSPR biosensing was published in 1998 by Englebienne,[4] who measured the plasmon peak position at equilibrium for different concentrations of antigen binding reversibly to the surface of antibody-functionalized Au colloids. Since then, a myriad of different prototype LSPR refractive index sensors have been used to detect biological interactions, following the pioneering work by van Duyne et al., and summarized in recent reviews.[5−7] The first nonmodel application of a LSPR refractive index sensor was demonstrated in 2004 by Haes et al., who studied the interaction between molecules possibly involved in Alzheimer's disease.[8,9] In the context of plasmonic biosensing, already early on, the capability and potential of single particle-based sensing was realized and demonstrated, for example, in 2003[10] by McFarland et al. by employing individual Ag nanoparticles as refractive index sensors with zeptomole sensitivity.

Nonbio applications of nanoplasmonic sensing started emerging slowly at a later stage. In 2006, Sirinakis et al. utilized Au−yttria-stabilized zirconia (YSZ) composite materials for surface plasmon resonance based high temperature detection of CO.[11] In 2007, Langhammer et al. introduced an LSPR-based scheme for hydrogen sensing,[12] which was followed in 2008 by Novo et al., who demonstrated the possibility of directly observing a redox reaction on the surface of single gold nanocrystals using LSPR spectroscopy[13] and by Rogers et al., who again used Au-YSZ nanocomposite films but now for plasmonic-based detection of NO_2 in a harsh environment.[14] The further development of nanoplasmonic sensing into a truly versatile in situ spectroscopy platform for materials science and catalysis applications was then pioneered by the authors[1,2,15−21] and has contributed significantly to the acceleration of research efforts in this novel research area. This is illustrated by recent successful efforts toward single-particle spectroscopy both by the authors[22] and by Alivisatos at al.[23,24] to probe the hydride formation in individual Pd nanoparticles and is further illustrated by other very interesting studies in which the LSPR of metallic nanoparticles was used as a local in situ probe to monitor processes in/on functional nanomaterials and catalysts.[25−31]

4. INDIRECT NANOPLASMONIC IN SITU SPECTROSCOPY FOR CATALYSIS APPLICATIONS

As briefly introduced above, the INPS spectroscopy platform utilizes the LSPR excitation in either individual or an array of plasmonic gold sensor particles at visible light frequencies to study processes and changes on/in adjacent nanomaterials. As the key novel ingredient to facilitating the use of LSPR-based sensors in highly demanding environments (as is typical for heterogeneous catalysis) and allowing for almost infinite material combinations, the INPS measurement principle features a dielectric spacer layer (a few to a few tens of nanometers thick) that physically separates the plasmonic sensor nanoparticles from the probed nanomaterial deposited on top. This arrangement is sketched schematically in Figure 2a and is illustrated for a specific system (that is, Pt nanoparticles on a 10 nm sputtered SiO_2 spacer layer) in the SEM micrographs in Figure 2b and c. Specifically, the spacer layer serves the following key functions: (i) the protection of the Au nanosensors from the environment and from structural reshaping/recrystallization at high temperature; (ii) a protection preventing the nanomaterial from directly interacting with the Au sensors by, for example, alloy formation; (iii) the possibility for tailored surface chemistry of the support material (either chemically inert or active) for the nanomaterial/catalyst to be studied; and (iv) a means to engineer the local field enhancement by tailoring the refractive index of the layer. In principle, any dielectric material that can be deposited as a thin flat or porous film, such as TiO_2, Si_3N_4, or Al_2O_3, transparent conductive oxides such as ZnO or ITO (for potential use in electrocatalysis), but also polymers, can be used as the spacer layer. In summary, the INPS sensor "chips" constitute a versatile platform that first is prepared according to the demands of a specific system to be studied and onto which the sample material is deposited in a subsequent step by, for example, evaporation of a granular film or by spin-coating, drop-casting, screen-printing, etc. of nanomaterial/particle suspensions or pastes.

For the experiment, the INPS chip with the sample material is mounted in a suitable reaction chamber, which allows for
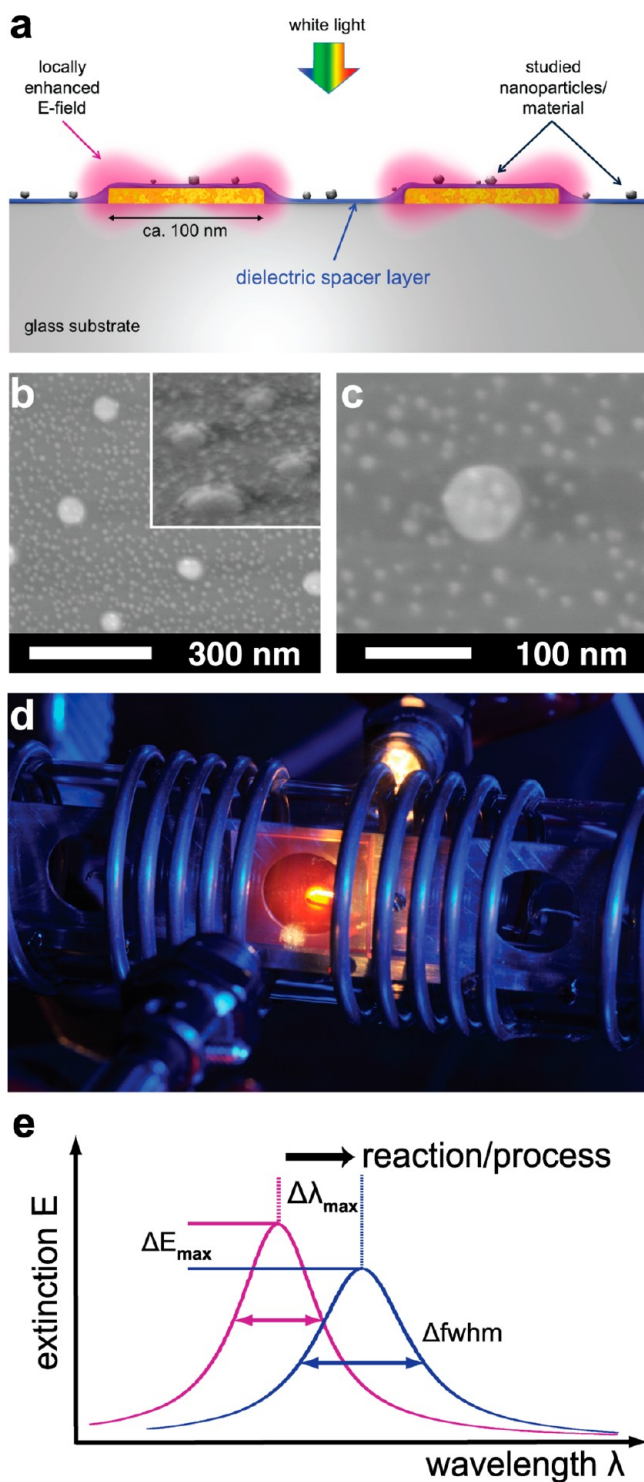
presence of the spacer layer. (d) Photograph of a possible arrangement for an INPS experiment in catalysis featuring a quartz tube flow reactor with a mounted INPS chip (red) and optical fibers for illumination and readout. The reactor is heated resistively by a heating coil and connected to a set of mass flow controllers, which operate the system at atmospheric pressure. (e) Schematic illustration of the readout from an INPS experiment. The wavelength of maximum extinction (the "peak") of the LSPR in the Au sensor particles, λ_{max}, is the main observable. Hence, it is spectral shifts, $\Delta\lambda_{max}$, induced by a process on/in the sample material on the sensor that provides the sensing function. As additional observables, changes in the peak full-width-at-half-maximum (Δfhwm) and in the extinction at peak (ΔE_{max}) can also be used and may either yield improved signal-to-noise ratio during an experiment or also, in some cases, provide additional information. Adapted with permission from ref 19. Copyright 2012 American Chemical Society and Insplorion AB.

either optical transmission or reflection measurements in combination with control of the chip environment. One such arrangement (an Inplorion X1 system shown with permission from Insplorion AB, Göteborg, Sweden) is shown in Figure 2d, comprising a photograph of a quartz tube flow reactor with a mounted INPS chip (red) and optical fibers for illumination and readout. The reactor is heated resistively by a heating coil and connected to a set of mass flow controllers, which operate the system at atmospheric pressure. Alternative arrangements not shown here but used in some of the examples discussed below are smaller measurement cells designed to operate in either vacuum and batch mode or in liquid environment. Such measurement cells may rely on reflected rather than transmitted light as the readout. Furthermore, it is worth mentioning that the use of INPS at pressures above 1 bar is also possible and only limited by the design of the used reactor, not by the chip itself. Hence, basically *identical* INPS sensor chips can be used in all of these different arrangements mentioned above. The latter very nicely illustrates one of the most striking features of the INPS technology: namely, its robustness and versatility in terms of measurement cell and readout design.

We now turn to a brief discussion of the signal readout during INPS spectroscopy. As mentioned in the introduction, the wavelength of maximum light extinction (the "peak") of the LSPR in the Au sensor particles, λ_{max}, is very sensitive to changes within the sensing volume that extends a few tens of nanometers from the sensor surface. As the main observable, it is the shift of λ_{max} that provides the sensing function (Figure 2e). It can, by utilizing the curve-fitting procedures introduced by Dahlin et al.,[32] be efficiently measured with a resolution of 0.01 nm under optimal conditions and by means of a simple pixel array spectrometer. This high resolution is possible (despite typical spectral resolutions of such spectrometers in the 1 nm range only) (i) because in an INPS experiment *relative* temporal *variations* of the peak position are of interest and not the absolute ones; (ii) because the LSPR peak has a width of 100 nm or more (it is thus much wider than the resolution limit of the spectrometer); and (iii) because the applied curve-fitting efficiently reduces noise, as detailed in the Dahlin paper.

As additional observables to the shifts of the spectral peak position ($\Delta\lambda_{max}$), changes in the peak full-width-at-half-maximum (Δfhwm, inversely proportional to the lifetime of the LSPR excitation and, hence, to the total damping of the system) and in the extinction at peak (ΔE_{max}) can also be used

Figure 2. (a) Schematic depiction of the INPS sensing platform, which utilizes the LSPR excitation either in individual or in an array of plasmonic gold sensor particles at visible light frequencies to study processes and changes on/in adjacent nanomaterials. This sensor "chip" features a dielectric spacer layer (a few to a few tens of nanometers thick) that physically separates the plasmonic Au sensor nanoparticles from the probed nanomaterial deposited on top. The spacer layer, which acts as a support for the probed sample material can be chosen freely form any dielectric that can be deposited as a thin compact layer. (b, c) SEM micrographs of an INPS sensor showing the amorphous array of Au nanodisk sensors and small (~10 nm) Pt nanoparticles (the sample material) on top. The inset in part b shows a side view SEM image (at a 70° tilt angle), clearly illustrating the

(Figure 2e). The latter may either yield improved signal-to-noise ratio during an experiment or also, in some cases (depending on the probed system; a specific example is discussed below in connection with Figure 7), provide additional information.[20]

After having advertised the particular benefits of the INPS technology, it is at this point also appropriate to highlight particular complications. The latter can be summarized by the fact that the readout simply corresponds to spectral shifts of the LSPR, which are attributed to a specific process in the probed material. In other words, the obtained signals are nonspecific and do not provide information about *which* process is being monitored unless it is either known from the beginning or determined by additional experiments by a complementary technique. This clearly highlights the importance of appropriate experimental design in cases that the sensing mechanism may be difficult to ascertain; that is, situations in which the occurrence of parallel reactions and interactions (e.g., with the spacer layer material) or temperature changes may convolute with the signal caused by the process to be studied. Typical measures to be taken to get rid of unwanted "background signals" are calibration measurements on blank sensor chips (without the studied nanomaterials of interest) and in inert/nonreacting gas atmosphere. Furthermore, "calibration" of the INPS signals by means of a complementary technique (e.g., by intermittent SEM/TEM imaging, XPS, QCM) or the direct combination of INPS with other probes (mass spectrometry, FTIR, QCM) might be necessary to distinguish among different contributions to the total INPS signal. In this sense, in more complex environments, INPS is probably most useful as a fast screening technique to probe in situ under which specific conditions a (at this point unspecified) process occurs. From the obtained information, more advanced experiments can then be derived, involving other techniques, to scrutinize the details of the process.

Finally, it is also relevant to briefly discuss the accessible temperature range for INPS and potential limitations of the latter. The highest temperature we have used successfully in an ongoing project (unpublished) is 850 °C, and the highest published temperature is 610 °C[19] (see Figure 4). We can identify a number of factors, principally limiting the accessible temperature range of INPS. The first one is naturally the melting temperature of the Au nanodisk sensors, which (if bulk behavior is assumed) is 1063 °C. Interestingly, however, as shown on experiments with Sn nanoparticles undergoing a melting and freezing transition,[33] the LSPR is not significantly affected by the transition to the liquid phase. Hence, it is possible that the sensing functionality would persist even in the liquid phase of the Au, provided that the liquid metal can be contained in the spacer layer cavity.

The latter indicates a second possible limitation (potentially relevant also below the Au melting temperature), which is diffusion of Au from the sensor particles into/through the dielectric layer, penetration of the sample material into the dielectric and even into the Au sensor, or both. The importance of such effects naturally depends on the specific material combinations chosen as well as on the chemical environment the INPS platform is exposed to.

A third potential limitation at very high temperatures might be the large damping of the LSPR due to efficient electron–phonon coupling,[34] which ultimately quenches the LSPR peak to such an extent that monitoring of spectral shifts becomes increasingly difficult. In essence, it becomes clear that it is quite

difficult to clearly define an upper temperature limit, since the latter strongly depends on the specific material combinations at hand. Hence, such limitations, if extreme temperatures are sought, have to be determined for each specific system individually.

We will now illustrate using a number of specific examples how INPS can be applied to probe supported nanocatalyst materials in situ and in harsh chemical environment. Our results clearly indicate that we can probe nanoparticles in the sub-10 nm range in situ, in real time, and at temperatures up to 610 °C in both reducing and oxidizing atmospheres to resolve chemical reactions and structural changes at the ensemble and the single particle level.

5. MONITORING ADSORBATE COVERAGE CHANGES AT ATMOSPHERIC PRESSURE ON A MODEL CATALYST

INPS can be used to monitor changes in adsorbed species on catalyst nanoparticles, as we have illustrated on the well studied Pt-catalyzed CO oxidation reaction.[2] For that purpose, an INPS sensor chip with a 10 nm SiO_2 spacer layer and Pt catalyst nanoparticles in the 5−20 nm size range (surface coverage of 20%) was used. The sample was exposed to mixtures of CO and O_2 in Ar carrier gas at atmospheric pressure with the total reactant concentration kept constant at 8%. The relative CO concentration, $\alpha^{CO} = [CO]/([CO] + [O_2])$, was scanned from CO-rich to O_2-rich and back while continuously recording the spectral position of the LSPR peak maximum, $\Delta\lambda_{max}$. The sample temperature was measured to 506 K in the absence of a reaction with a thermocouple in contact with the sample surface.

When scanning the relative CO concentration, discontinuous steps up and down (depending on whether the CO fraction was increasing or decreasing) of ~1 nm in $\Delta\lambda_{max}$ at a critical reactant mixture of α_{cr}^{CO} around 0.07 were observed (blue curves in Figure 3 a). The $\Delta\lambda_{max}$ step is assigned to the kinetic phase transition in the CO + O_2 reaction, occurring at a critical gas mixture, where a sudden transition occurs from an oxygen-covered surface at low α^{CO} to a CO-covered surface at high α^{CO}. This transition occurs where the overall exothermic reaction has a rate maximum, which is the reason for the measured peak in temperature (red curves in Figure 3a). The asymmetry of the temperature versus α profile around α_{cr}^{CO} is due to the well-known poisoning effect of CO for oxygen adsorption, preventing O_2 from dissociating and reacting. A very similar experiment for the $H_2 + (1/2)O_2 \rightarrow H_2O$ reaction is also discussed in our original paper.[2] As the main conclusion, these examples demonstrate that INPS can detect surface coverage changes at the submonolayer level on a supported nanoparticle catalyst at atmospheric pressures (and potentially above). It furthermore implies that coverage changes on real catalyst structures (that is, catalyst nanoparticles dispersed on a porous washcoat material) can be monitored using INPS if the sensor structure is modified accordingly.[18]

6. MONITORING NO$_X$ STORAGE KINETICS IN BARIUM OXIDE NO$_X$ ABATEMENT MODEL CATALYSTS

The next example is a practically important reaction in automotive emission cleaning for diesel and "lean burn" engines, that is, engines operated at oxygen excess, in which the conventional 3-way catalyst cannot reduce NO_x efficiently. This limitation has led to the development of so-called NO_x
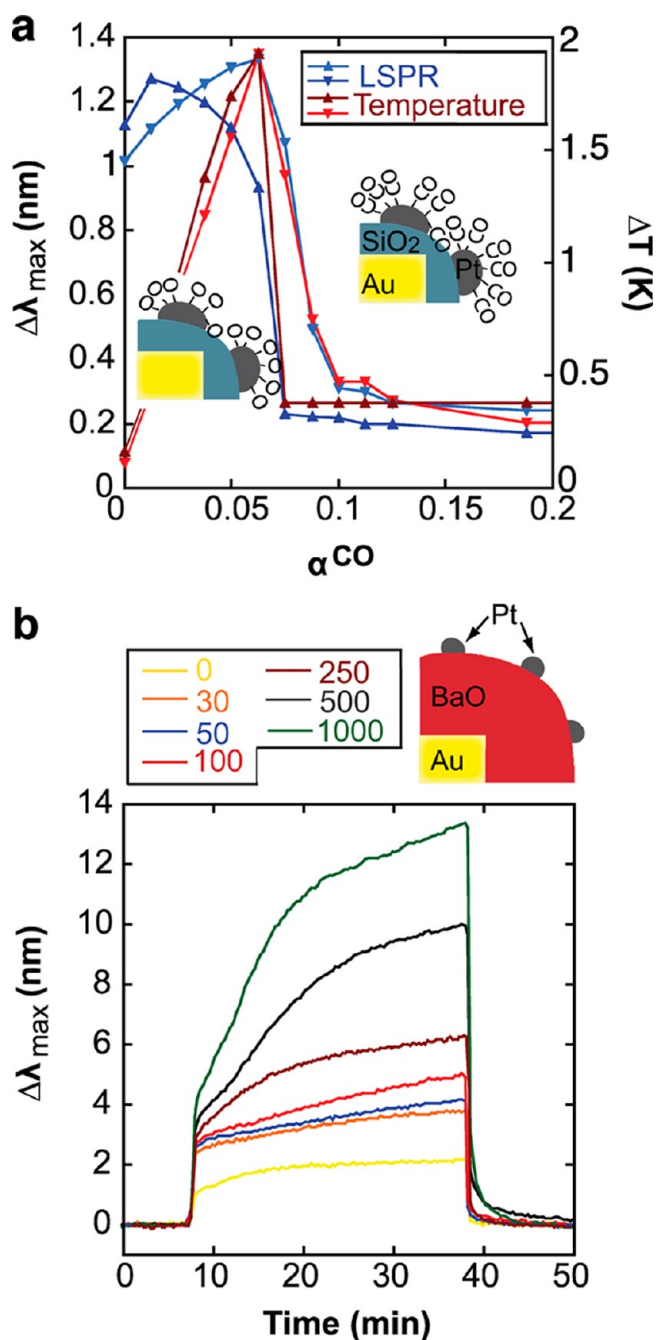
Figure 3. (a) Plasmon peak shift (blue) and temperature variation (red) during relative CO concentration in the gas mixture, α^{CO}, sweeps. The triangles pointing up and down represent a sweep up and down, respectively. The schematic illustrations to the left and right of the step in $\Delta\lambda_{max}$ illustrate the change in surface coverage upon passing the kinetic phase transition for α^{CO} sweeps at 506 K, 8% CO + O$_2$ reactant concentration, and 16.7 mL/s gas flow rate. (b) NO$_x$ storage and release kinetics from BaO measured with the INPS arrangement as schematically depicted in the top right corner. The $\Delta\lambda_{max}$ response during 30 min NO$_2$ storage (at t = 8 to 38 min) for seven different NO$_2$ concentrations (0, 30, 50, 100, 250, 500, and 1000 ppm) and subsequent release by exposure to 2% H$_2$ (at t = 38 min) is shown. Adapted with permission from ref 2.

storage/reduction catalysts. The most commonly used NO$_x$ storage material is barium oxide (BaO), which upon NO$_x$ storage is converted to Ba(NO$_3$)$_2$ or related compounds. Pt (and, in practice, usually also Rh) is needed for the reduction

step (conversion of Ba(NO$_3$)$_2$ to BaO or BaCO$_3$ with the release of N$_2$ and also for oxidation of NO (when present) to NO$_2$ during the storage phase.

In our model experiment, INPS was used to monitor the NO$_x$ storage in and release from BaO by replacing the passive spacer layer with a ~30-nm-thick BaO layer on top of which a nanogranular Pt film (nominal thickness 0.5 nm, yielding particles in the few nanometers size range) was deposited.[2] To mimic the NO$_x$ storage period, the sample was exposed for 30 min to a gas mixture of 30−1000 ppm NO$_2$ + 6% O$_2$. It was subsequently exposed to 2% H$_2$ to mimic the reduction period. During the NO$_2$ storage cycle, the INPS sensor responds with an initial rapid upward shift of $\Delta\lambda_{max}$ within 20 s and then a slowly continuing increase, which is greater for higher NO$_2$ concentrations (see Figure 3b). Exposing the sample to H$_2$ (at 38 min in Figure 3b) results, as expected, in a shift of $\Delta\lambda_{max}$ back to the original value before the NO$_2$ exposure because of the hydrogen reduction of stored NO$_x$ to N$_2$ and concerted Ba(NO$_3$)$_2$ → BaO conversion.

7. REAL-TIME INDIRECT NANOPLASMONIC IN SITU SPECTROSCOPY OF CATALYST NANOPARTICLE SINTERING

Catalyst sintering is the coalescence of catalyst particles with concomitant loss of surface area and activity. The applicability of INPS to monitor catalyst sintering was demonstrated by the authors using the Pt/SiO$_2$ system.[19] Figure 4a shows the optical absorbance spectra obtained at different time intervals from an INPS sensor with a 10 nm SiO$_2$ spacer layer during the sintering of Pt nanoparticles (average size 3.3 ± 1.1 nm) in 4% O$_2$ (in Ar) at 610 °C. Clearly, as the Pt nanoparticles undergo significant sintering, the LSPR peak shifts toward shorter wavelengths and, simultaneously, a decrease in the optical absorbance is observed. To correlate the INPS readout signal, $\Delta\lambda_{max}$, with the sintering of the Pt nanoparticles, experiments were performed in which the sintering process was interrupted after different exposure times to 4% O$_2$/Ar atmosphere at 550 °C (Figure 4b; notice the reproducibility between the different experiments) and correlated with TEM images obtained intermittently after each sintering time interval (Figure 4 c).

From these data, to analyze and quantify the sintering kinetics measured with INPS, the $\Delta\lambda_{max}$ signal can be correlated with the structural/size changes of the catalyst particles during the sintering process. This is illustrated in Figure 4d, where the $\Delta\lambda_{max}$ values from the sintering experiments shown in Figures 4a−c (but also additional measurements obtained at different temperatures and shown in ref 19) are plotted versus the Pt particle density, P, on the sensor surface, as obtained from TEM image analysis. Clearly, a direct linear correlation between the two parameters is found. Through a subsequent derivation of an empirical calibration function, the particle density can be translated into an average particle diameter, which directly links the INPS signal $\Delta\lambda_{max}$ to the particle size. Hence, the time-resolved INPS readout signal could be used to scrutinize the nanoparticle sintering process in situ by further analysis and quantification. For the particular case investigated in our first study (that is, Pt nanoparticles on SiO$_2$), fitting of an analytical kinetic model to the experimentally obtained data yielded excellent agreement for parameters implying Ostwald ripening with the detachment activation energy dependent on the particle size as the main sintering mechanism.
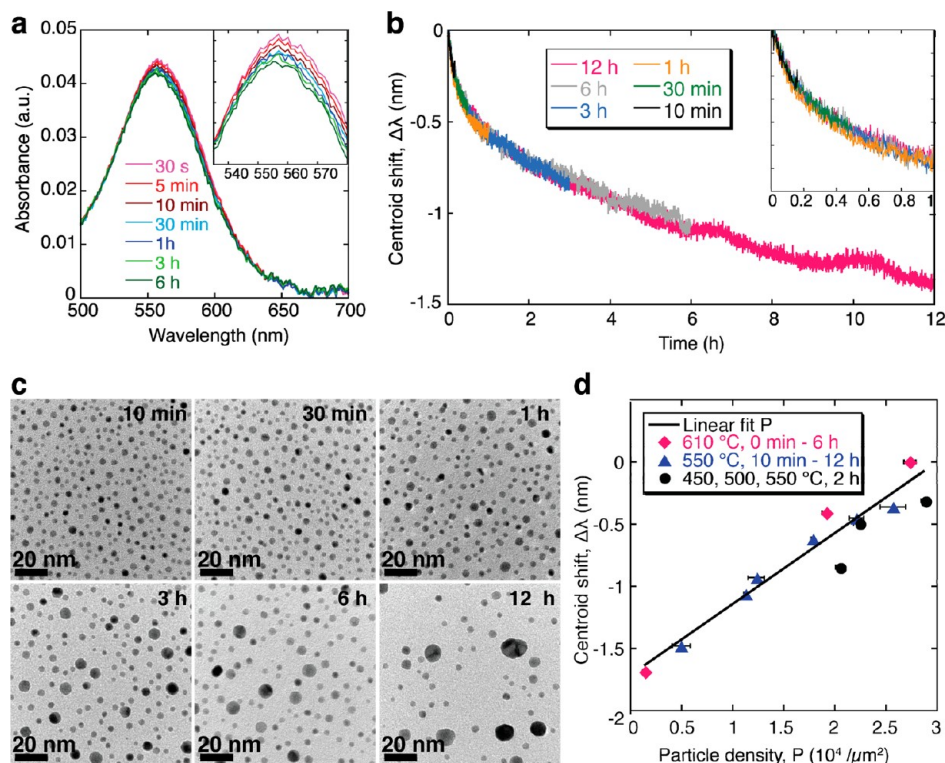
Figure 4. INPS sensor response to model catalyst sintering. (a) Absorbance spectra from the INPS sensor obtained at different times during the sintering of the Pt model catalyst in 4% O_2/Ar at 610 °C. The LSPR peak of the INPS sensor spectrally shifts to the blue, and simultaneously, a decrease in the optical absorbance is observed. (b) Real time plasmonic sintering kinetic curves obtained for six different samples and sintering times under identical experimental conditions (4% O_2/Ar atmosphere at 550 °C) demonstrate very good reproducibility between experiments. (c) Corresponding TEM micrographs obtained after each sintering time interval; that is, 10 min, 30 min, 1 h, 3 h, 6 h, and 12 h, clearly illustrate the significant sintering of the Pt model catalyst, as registered by the INPS sensor. (d) $\Delta\lambda_{max}$ versus the Pt particle density, P, on the sensor surface, as obtained from TEM image analysis for three different measurement series obtained at different temperatures. The black solid line corresponds to a linear regression fit yielding an empirical calibration curve: $\Delta\lambda_{max} = -1.71 + (5.69 \times 10^{-5})P$. Adapted with permission from ref 19. Copyright 2012 American Chemical Society.

8. OXIDATION AND REDUCTION OF PALLADIUM NANOPARTICLES

The catalytic activity of a particular metal nanoparticle usually depends on its oxidation state. However, the oxidation state of catalysts during reaction conditions is often unknown because of the lack of available techniques to monitor changes in the oxidation state at realistic catalyst working conditions. In the next example, INPS was used to monitor the oxidation and reduction kinetics of Pd nanoparticles supported on 10 nm Si_3N_4 at atmospheric pressure.

The INPS signal, $\Delta\lambda_{max}$, upon oxidation (100 ppm O_2 in Ar at atmospheric pressure) and subsequent reduction (2% H_2 in Ar) of Pd nanoparticles at 208 °C is shown in Figure 5b, together with the response from a blank sensor. The Pd nanoparticles were formed by electron beam evaporation of granular Pd films with nominal thicknesses 0.1 and 0.5 nm and subsequent thermal annealing (5 h in air at 450 °C), followed by oxidation−reduction cycles. The resulting average particle diameters were 1.2 nm (part a, left) and 3.1 nm (part b, right), respectively. Oxidation of the Pd nanoparticles caused a red shift of $\Delta\lambda_{max}$ of 0.07 nm for the 1.2 nm particles and 0.39 nm for the 3.1 nm particles; that is, a 5.6 times larger peak shift was observed for the larger ones. The latter corresponds well to the total amount of Pd on the samples, which was 5 times larger on the sample with the 3.1 nm particles than on the sample with the 1.2 nm particles. This is a strong indication that the Pd

nanoparticles are completely oxidized in 100 ppm O_2 and then completely reduced in 2% H_2 at 208 °C.

The complete oxidation of Pd particles <3 nm in diameter has previously been observed upon oxygen exposure at 500 K using molecular beam experiments,[35] supporting this interpretation. These data thus represent a first convincing indication that INPS can be used to monitor the oxidation state and oxidation/reduction kinetics of catalyst nanoparticles. Furthermore they could constitute a first step in a more advanced experiment in which the oxidation state of the catalyst is determined first, in situ, followed by scrutiny of the catalytic activity of the particles in the oxidized or reduced state by optical nanocalorimetry, as described below or by complementary readout with, for example, a mass spectrometer.

9. INPS-BASED LOCAL TEMPERATURE READOUT FOR OPTICAL NANOCALORIMETRY

Our next example illustrates the possibility to use INPS to measure local temperature changes at the nanoscale (that is, the temperature of the catalyst nanoparticles, not the average temperature of the entire catalyst system, including the support structure) and how this intrinsic temperature sensitivity of LSPR[34] can be utilized in optical nanocalorimetry[1] experiments. Figure 6 a depicts the typical $\Delta\lambda_{max}$ vs T characteristics of the INPS sensor chip upon external heating; that is, a linear T dependence and a temperature sensitivity of $\Delta\lambda_{max} = 0.0125$ nm/°C.
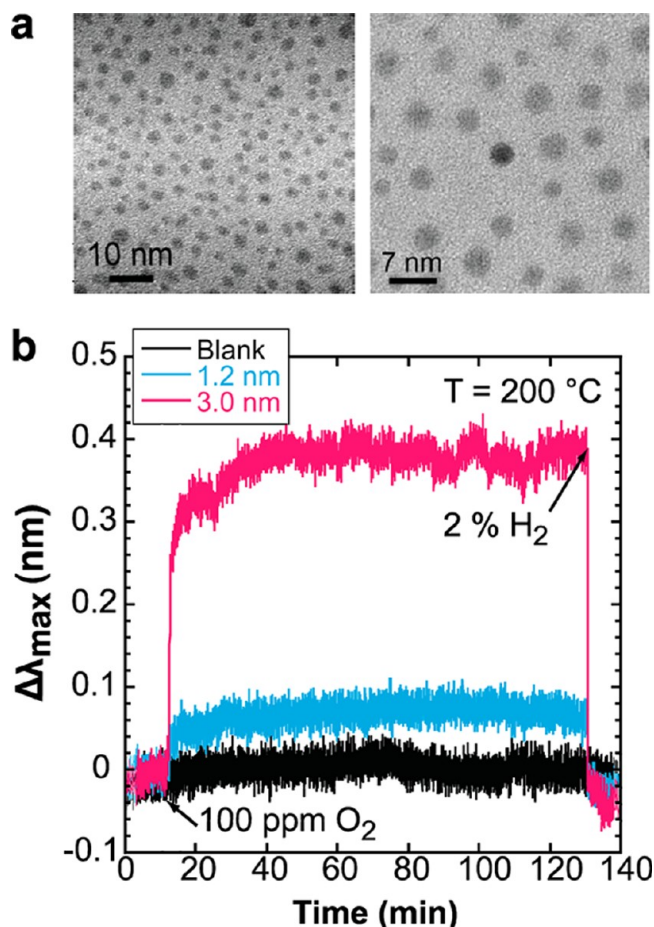
a

b

Figure 5. Pd nanoparticle oxidation and reduction kinetics. (a) TEM pictures of the studied Pd nanoparticles with average diameters of 1.2 (left) and 3.1 nm (right). They were formed by electron beam evaporation of granular Pd films and subsequent thermal annealing (5 h in air at 450 °C). (b) INPS signal upon oxidation (100 ppm O_2 in Ar at atmospheric pressure) and subsequent reduction (2% H_2 in Ar) of the Pd nanoparticles shown in part a at 208 °C. The particles are supported on a Si_3N_4 spacer layer. The response to the oxidizing and reducing gases from a blank sensor is also shown. Oxidation of the Pd nanoparticles caused a spectral red-shift of $\Delta\lambda_{max}$ of 0.07 nm for the 1.2 nm particles and 0.39 nm for the 3.1 nm particles, in agreement with a 5-times-larger amount of Pd on the sample with the 3.1 nm particles. This is a strong indication that the Pd nanoparticles are completely oxidized during the experiment.

For the calorimetry experiment, we use the exothermic $H_2 + (1/2)O_2 \rightarrow H_2O$ reaction over Pd nanoparticles as our model reaction and make use of the fact that the energy released on the Pd nanoparticles causes a temperature rise on the sample surface and of the sensing Au nanodisks, which, in turn, causes a spectral shift of the LSPR peak. By relying on the calibrated temperature dependence of $\Delta\lambda_{max}$, the local temperature rise caused by the reaction can be obtained. We notice here that this assumes that the chemical properties of the catalyst surface stay unchanged (that is, that no surface oxidation or kinetic phase transition, as discussed above, takes place); otherwise, such changes may add to the observed spectral shift. For the experiments presented below, both the chosen temperatures and gas compositions should guarantee the absence of such interfering signals.

During the experiment, the sample temperature is increased by a linear temperature ramp of the reactor. During such a T
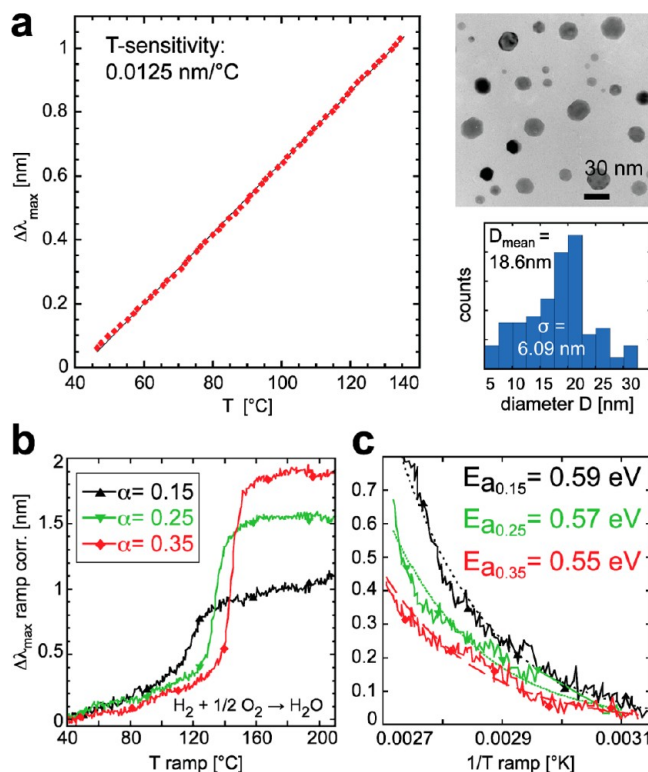
a

b   **c**

Figure 6. (a) Depiction of the linear T dependence of the $\Delta\lambda_{max}$ signal, yielding a temperature sensitivity of $\Delta\lambda_{max} = 0.0125$ nm/°C (left), and a TEM image with corresponding size distribution histogram of the investigated Pd nanoparticles with $\langle D \rangle = 18.6$ nm (right). (b) Catalytic light-off traces obtained for the hydrogen oxidation for $\alpha = 0.15, 0.25, 0.35$, where α is defined as $\alpha = [H_2]/([H_2] + [O_2])$, in Ar carrier gas at 4% total reactant concentration. The displayed $\Delta\lambda_{max}$ values correspond to local heating of the Au sensor nanodisks by the exothermic reaction ($\Delta H = 250$ kJ/mol). (c) Arrhenius analysis of LSPR temperature traces below light-off (the dotted/dashed lines correspond to Arrhenius function fits to the LSPR data), yielding slightly different apparent activation energies for the different α values. Adapted with permission from ref 1. Copyright 2010 American Chemical Society.

sweep, at low catalyst temperatures, when the reaction is slow enough to not be limited by mass transport, the reaction rate and the associated dissipated chemical power are kinetically limited and, thus, governed by Arrhenius-like kinetics. Upon further temperature increase, the system reaches and passes through a transient regime where a transition takes place from kinetically controlled to mass-transport-controlled conditions that are governed by concentration gradients. This transition between two regimes (also referred to as light-off or ignition) yields a typical S-like curve of the reaction rate versus temperature.

Figure 6 b shows such catalytic light-off traces obtained by INPS for Pd nanoparticles with $\langle D \rangle = 18.6$ nm at three different relative H_2 and O_2 concentrations in Ar carrier gas ($\alpha = [H_2]/([H_2] + [O_2])$) at atmospheric pressure and constant total reactant concentration (4%). The reactor heating rate was 4 °C/min, and the constant gas flow rate was 1000 mL/min. The displayed $\Delta\lambda_{max}$ values are corrected for the peak shift induced by the *external* heating of the reactor by using the calibration curve in Figure 6a. If there were no heat source other than the external heating, the three curves would, thus, be completely flat. The rise over the abscissa can therefore be

attributed to the *local* heating from the exothermic $H_2 + (1/2)O_2 \rightarrow H_2O$ reaction ($\Delta H = -250$ kJ/mol) on the Pd catalyst particles. As expected, the reaction-induced temperature rise increases with increasing reactor temperature (T_{ramp}) as a result of the Arrhenius type temperature dependence of the reaction.

The general shape of the obtained curves is in very good agreement with the general considerations above (S-curve). In the early part of the curve, the surface of the catalyst is predominantly covered with dissociated hydrogen (despite the oxygen excess in the gas mixture) because of the significantly higher sticking coefficient at the considered temperature. This means that the catalyst is in the reduced/metallic state, and no Pd surface oxidation, potentially convoluting the LSPR signal, is expected to take place.[36] The observed trend that the light-off is occurring at higher temperatures for higher α values is also as expected and has its origin in the detailed kinetics of the reaction, which can be related to hydrogen poisoning and that the apparent reaction activation energy can be associated with hydrogen desorption.[36]

As the final step for the analysis presented here (for further details, we refer to the original paper[1]), an Arrhenius analysis of the low-temperature (below light-off) regime is shown in Figure 6c. The obtained apparent activation energies for three different reactant concentrations are in excellent agreement with the literature[37,38] and demonstrate the potential of nanoplasmonic sensing in general and of INPS in particular as an optical nanocalorimetry tool in catalysis.

10. SINGLE PARTICLE INPS SPECTROSCOPY

As the last example and to illustrate the potential of nanoplasmonics-based spectroscopy for probing individual nanoparticles in situ under application conditions, we discuss briefly a recent study of the hydride formation thermodynamics in single Pd nanoparticles in the sub-30 nm size range. In this context, it is illustrative to recall that the introduction of dark-field scattering spectroscopy (DFSS) had made it possible to study the optical/plasmonic properties of single nanoparticles and to study the effects of particle size and particle shape[39] as well as the refractive index of the surrounding medium[7] at the single particle level; the latter, however, with the significant limitation to (i) particle sizes $D > 30-50$ nm (Rayleigh scattering is proportional to D,[6] indicating that small particles do not scatter light efficiently) and (ii) to Au and Ag only, owing to their favorable permittivity in the visible, that is, low losses and efficient scattering. Thus, nanoparticles consisting of other metals that typically feature larger imaginary dielectric functions (= high losses via light absorption) in the near-visible spectral range, like many catalytically active transition metals, have not been possible to investigate by DFSS. The above is very unfortunate in the sense that many functional nanosystems either are nonmetallic (and thus do not exhibit LSPR at all) or consist of metals featuring highly absorptive LSPRs and are only of interest and functional at sizes $D < 30$ nm.

In our study,[22] we circumvented this problem by following the general INPS concept and by using a novel sensor-probed nanoparticle geometry, namely, truncated Au nanocones with functionalized "tips" that could conveniently be fabricated in one physical vapor deposition step (Figure 7a). The structures can be used for single particle DFSS measurements on nanoparticles that are <30 nm and consist of absorptive metals or even dielectric materials which themselves don't support LSPR. Using this specific nanoarchitecture in a DFSS experiment, the truncated Au nanocone acts as a plasmonic
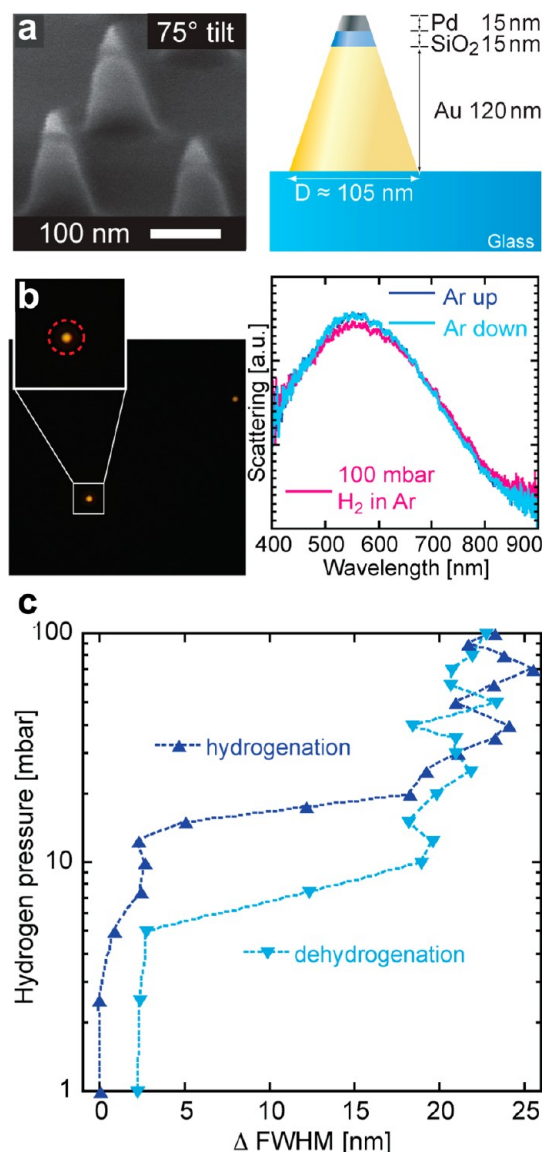

Figure 7. (a) SEM image (left) and schematic depiction (right) of an approximately 120-nm-high truncated Au nanocone with a 15-nm-thick SiO_2 spacer layer and a Pd particle with approximate dimensions of 30 nm × 15 nm at the tip. (b) Dark field scattering image of a single nanocone (left) and its spectral response to subsequent exposure to 100% Ar, 10% H_2 in Ar, and then 100% Ar (right) at room temperature. (c) Corresponding optical pressure−composition isotherm of the hydrogenation of a single Pd nanoparticle measured at 23 °C. Adapted with permission from ref 22. Copyright 2011 Wiley-VCH Verlag GmbH & Co.

sensor and as a strong light scatterer at the same time, which probes, through its enhanced plasmonic field, the adjacent functional but now not necessarily plasmonic and/or scattering nanoparticle deposited onto the spacer layer on the tip. By fine-tuning the fabrication parameters (that is, the amount/thickness of the deposited "tip" materials and total height of the structure), the size of the active nanoparticle sitting on the tip of the Au nanocone sensor can be controlled very accurately, and more complex structures featuring multiple layers of different materials are easily possible, as shown in the original paper. Other sensor-probed particle arrangements, such as core−shell structures[24] or a tailored nanofocus,[23] were

suggested and successfully utilized by Alivisatos and Giessen et al. for the same purpose and follow the general idea of INPS.

Figure 7b shows a dark-field scattering microscope image of a single truncated Au/SiO$_2$/Pd nanocone (left) and its spectral response from subsequent exposure to 100% Ar; 10% H$_2$ in Ar; and, again, 100% Ar (right) at atmospheric pressure; and at room temperature. A very clear and reversible shift of the LSPR peak in the scattering spectrum induced by transformation of the Pd particle at the tip of the nanocone into Pd hydride (PdH$_x$) can be resolved.

The result of a more systematic experiment is shown in Figure 7c, which comprises the optical pressure−composition isotherm of hydrogen in a single Pd nanoparticle, with a (base) diameter of only ∼30 nm and a thickness of 15 nm. It was obtained by reading out the change in full-width-at-half-maximum (Δfwhm) of the LSPR peak of the Au nanocone structure as a function of hydrogen partial pressure, p. The isotherms show the expected distinct α- (hydrogen in solid solution), $\alpha + \beta$ ("plateau", mixed phase), and β-phase (hydride) regions as characteristic for metal−hydrogen systems. A clear hysteresis between the sorption and desorption branches is also seen. We note that previous experimental and theoretical considerations of LSPR-based measurements of hydride formation in Pd nanosystems yielded a clear linear scaling of the LSPR signal with the hydrogen concentration in the Pd nanoparticles.[1,15] Hence, we can assume linearity even in these single particle experiments and correlate Δfwhm directly with the hydrogen concentration in the Pd nanoparticle. How these optical isotherms thus can be used to determine thermodynamic parameters such as the enthalpy of formation is further discussed in the original article and a number of other studies.[1,15,16,40]

As a final comment, we note that, as indicated in the introduction, the use of Δfwhm as a readout parameter for this particular experiment was motivated by a significantly larger shift compared with Δλ_{max}. This effect is caused by the fact that, during hydride formation in Pd, two separate contributions to the plasmonic response of the Au sensor exist and that they induce a shift of opposite sign in Δλ_{max}, which creates a situation in which the two basically cancel out each other. The two competing signals are a spectral blue shift caused by dielectric function changes in the Pd and a red shift due to an expansion of the Pd lattice during hydride formation.[41]

11. SUMMARY AND CONCLUSIONS

Indirect nanoplasmonic sensing, INPS, as the key step forward, facilitates the use of nanoplasmonic sensor technology in highly demanding environments in terms of temperature (up to 850 °C, so far), chemical harshness (strongly oxidizing and reducing atmospheres), and pressure for in situ and real time probing of catalyst and other functional nanomaterials. Furthermore, INPS allows for almost infinite material combinations. We also note that the pressure range within INPS can be used is not limited by the sensor or readout principle itself, but rather, by the design of the measurement cell; hence, experiments above atmospheric pressure should be straightforward.

The INPS sensor chip features a dielectric spacer layer physically separating the nanoplasmonic sensors from the probed nanomaterial and serving several additional key functions, including (i) protection of the Au nanosensors from the environment and from structural reshaping at high temperature, (ii) providing tailored surface chemistry (support material) for the nanomaterial/catalyst to be studied, (iii) being

chemically inert or (iv) participating actively in the process under study, e.g., in spillover effects during a catalytic reaction. In principle, any other dielectric material (oxides, nitrides, carbides) that can be deposited as a thin flat or porous film— but also polymers—can be used as the spacer layer/support material for an INPS experiment, depending on the needs of the specific probed system.

To date, we have successfully applied the INPS sensing platform to investigate structural and chemical changes of nanomaterials, such as in catalyst sintering processes,[19] the oxidation/reduction of Pd nanoparticles, or the storage of NO$_x$ species in BaO. We have also applied INPS to scrutinize size effects in the hydride formation process in nanoparticles in the sub-10 nm size range[1,16] or to measure in situ changes in adsorbate surface coverage on heterogeneous catalysts at atmospheric pressure.[2] Optical nanocalorimetry has been used to measure local temperature changes at the nanolevel and relate the latter, for example, to the activity of a catalyst.[1]

Furthermore, we have recently applied INPS to study dye molecule adsorption/impregnation of 10-μm-thick mesoporous TiO$_2$ photoanodes in dye-sensitized solar cells by placing the INPS sensor at the hidden, internal interface between the support and the mesoporous TiO$_2$.[18] This approach provides a unique opportunity to selectively follow dye adsorption *locally* in the hidden interface region *inside* the material and inspires a generic and new type of nanoplasmonic hidden interface spectroscopy that makes highly time-resolved measurements inside a material possible. This first application of hidden interface INPS has thus also prepared grounds for studies of even more realistic catalyst structures comprising a micro-meters-thick mesoporous washcoat-like support structure on the INSP chip, loaded with "real" catalyst nanoparticles. Finally, we have also demonstrated first experiments toward single particle INPS spectroscopy in the example of hydride formation in individual Pd and Mg nanoparticles.

In summary, owing to its sensitivity, versatility, robustness, compatibility with harsh environments and high temporal resolution in the millisecond range, INPS constitutes a very promising novel experimental platform for the in situ spectroscopy of functional nanomaterials such as catalysts under close-to or real application conditions. The lack of specificity of the readout signal, that is, shifts in the spectral position of the localized plasmon peak of the INPS sensor, requires careful design of experiments and, in some cases, combinations with complementary techniques, such as AFM/SEM/TEM, or other spectroscopic techniques, such as XPS. Hence, as one important future direction for further development, we identify the direct integration of the INPS function on a sample compatible with simultaneous additional readouts (such as the aforementioned ones but also others, such as quartz crystal microbalance,[42] or nonlinear optical spectroscopies, such as SFG) as a high priority. Furthermore, we believe that more efforts directed toward the probing of individual catalyst nanoparticles during a catalytic reaction are well motivated, because of both the promising first proof-of-principle experiments already presented and the potential to efficiently circumvent inhomogeneous sample material artifacts. As the main challenges, here, we identify on one hand the optimization of the utilized microspectroscopy for compatibility with high temperatures and, on the other hand, the further optimization of sensitivity and geometrical arrangement of sensor and probed nanoparticle to ultimately be able to probe

individual nanoparticles in the sub-10 nm size range under realistic application conditions.

■ **AUTHOR INFORMATION**

Corresponding Author

*E-mail: clangham@chalmers.se.

Notes

The authors declare no competing financial interest.

■ **REFERENCES**

(1) Langhammer, C.; Larsson, E. M.; Kasemo, B.; Zoric, I. *Nano Lett.* **2010**, *10* (9), 3529−3538.

(2) Larsson, E. M.; Langhammer, C.; Zoric, I.; Kasemo, B. *Science* **2009**, *326* (5956), 1091−1094.

(3) Bohren, C. F.; Huffman, D. R. *Absorption and Scattering of Light by Small Particles*; Wiley-Interscience: New York, 1983.

(4) Englebienne, P. *Analyst* **1998**, *123* (7), 1599−1603.

(5) Haes, A. J.; Haynes, C. L.; McFarland, A. D.; Schatz, G. C.; Van Duyne, R. R.; Zou, S. L. *MRS Bulletin* **2005**, *30* (5), 368−375.

(6) Lal, S.; Link, S.; Halas, N. J. *Nat. Photonics* **2007**, *1* (11), 641−648.

(7) Anker, J. N.; Hall, W. P.; Lyandres, O.; Shah, N. C.; Zhao, J.; Van Duyne, R. P. *Nat. Mater.* **2008**, *7* (6), 442−453.

(8) Haes, A. J.; Chang, L.; Klein, W. L.; Van Duyne, R. P. *J. Am. Chem. Soc.* **2005**, *127* (7), 2264−2271.

(9) Haes, A. J.; Hall, W. P.; Chang, L.; Klein, W. L.; Van Duyne, R. P. *Nano Lett.* **2004**, *4* (6), 1029−1034.

(10) McFarland, A. D.; Van Duyne, R. P. *Nano Lett.* **2003**, *3* (8), 1057−1062.

(11) Sirinakis, G.; Siddique, R.; Manning, I.; Rogers, P. H.; Carpenter, M. A. *J. Phys. Chem. B* **2006**, *110* (27), 13508−13511.

(12) Langhammer, C.; Zoric, I.; Kasemo, B.; Clemens, B. M. *Nano Lett.* **2007**, *7* (10), 3122−3127.

(13) Novo, C.; Funston, A. M.; Mulvaney, P. *Nat. Nanotechnol.* **2008**, *3* (10), 598−602.

(14) Rogers, P. H.; Sirinakis, G.; Carpenter, M. A. *J. Phys. Chem. C* **2008**, *112* (24), 8784−8790.

(15) Zoric, I.; Larsson, E. M.; Kasemo, B.; Langhammer, C. *Adv. Mater.* **2010**, *22* (41), 4628−4633.

(16) Langhammer, C.; Zhdanov, V. P.; Zoric, I.; Kasemo, B. *Phys. Rev. Lett.* **2010**, *104* (13), 135502.

(17) Langhammer, C.; Schwind, M.; Kasemo, B.; Zoric, I. *Nano Lett.* **2008**, *8* (5), 1461−1471.

(18) Gusak, V.; Heiniger, L.-P.; Graetzel, M.; Langhammer, C.; Kasemo, B. *Nano Lett.* **2012**, *12* (5), 2397−2403.

(19) Larsson, E. M.; Millet, J.; Gustafsson, S.; Skoglundh, M.; Zhdanov, V. P.; Langhammer, C. *ACS Catal.* **2012**, *2* (2), 238−245.

(20) Schwind, M.; Langhammer, C.; Kasemo, B.; Zoric, I. *Appl. Surf. Sci.* **2011**, *257* (13), 5679−5687.

(21) Shegai, T.; Johansson, P.; Langhammer, C.; Kall, M. *Nano Lett.* **2012**, *12* (5), 2464−2469.

(22) Shegai, T.; Langhammer, C. *Adv. Mater.* **2011**, *23* (38), 4409−4414.

(23) Liu, N.; Tang, M. L.; Hentschel, M.; Giessen, H.; Alivisatos, A. P. *Nat. Mater.* **2011**, *10*, 631−636.

(24) Tang, M. L.; Liu, N.; Dionne, J. A.; Alivisatos, A. P. *J. Am. Chem. Soc.* **2011**, *133* (34), 13220−13223.

(25) Huang, X.; Tang, S.; Mu, X.; Dai, Y.; Chen, G.; Zhou, Z.; Ruan, F.; Yang, Z.; Zheng, N. *Nat. Nanotechnol.* **2011**, *6* (1), 28−32.

(26) Szwarcman, D.; Vestler, D.; Markovich, G. *ACS Nano* **2011**, *5* (1), 507−515.

(27) Dahlin, A. B.; Sannomiya, T.; Zahn, R.; Sotiriou, G. A.; Voros, J. *Nano Lett.* **2011**, *11* (3), 1337−1343.

(28) Joy, N. A.; Settens, C. M.; Matyi, R. J.; Carpenter, M. A. *J. Phys. Chem. C* **2011**, *115* (14), 6283−6289.

(29) Seo, D.; Park, G.; Song, H. *J. Am. Chem. Soc.* **2012**, *134* (2), 1221−1227.

(30) Borensztein, Y.; Delannoy, L.; Djedidi, A.; Barrera, R. G.; Louis, C. *J. Phys. Chem. C* **2010**, *114* (19), 9008−9021.

(31) Lei, D. Y.; Appavoo, K.; Sonnefraud, Y.; Haglund, J. R. F.; Maier, S. A. *Opt. Lett.* **2010**, *35* (23), 3988−3990.

(32) Dahlin, A. B.; Tegenfeldt, J. O.; Höök, F. *Anal. Chem.* **2006**, *78* (13), 4416−4423.

(33) Schwind, M.; Zhdanov, V. P.; Zoric, I.; Kasemo, B. *Nano Lett.* **2010**, *10* (3), 931−936.

(34) Liu, M.; Pelton, M.; Guyot-Sionnest, P. *Phys. Rev. B* **2009**, *79* (3), 035418.

(35) Schalow, T.; Brandt, B.; Starr, D. E.; Laurin, M.; Shaikhutdinov, S. K.; Schauermann, S.; Libuda, J.; Freund, H.-J. *Angew. Chem., Int. Ed.* **2006**, *45* (22), 3693−3697.

(36) Fassihi, M.; Zhdanov, V. P.; Rinnemo, M.; Keck, K. E.; Kasemo, B. *J. Catal.* **1993**, *141* (2), 438−452.

(37) Rinnemo, M.; Fassihi, M.; Kasemo, B. *Chem. Phys. Lett.* **1993**, *211* (1), 60−64.

(38) Johansson, Å.; Försth, M.; Rosen, A. *Int. J. Mol. Sci.* **2001**, *2* (5), 221−229.

(39) Novo, C.; Gomez, D.; Perez-Juste, J.; Zhang, Z. Y.; Petrova, H.; Reismann, M.; Mulvaney, P.; Hartland, G. V. *Phys. Chem. Chem. Phys.* **2006**, *8* (30), 3540−3546.

(40) Langhammer, C.; Zhdanov, V. P.; Zoric, I.; Kasemo, B. *Chem. Phys. Lett.* **2010**, *488*, 62−66.

(41) Tittl, A.; Kremers, C.; Dorfmuller, J.; Chigrin, D. N.; Giessen, H. *Opt. Mater. Express* **2012**, *2* (2), 111−118.

(42) Larsson, E. M.; Edvardsson, M. E. M.; Langhammer, C.; Zoric, I.; Kasemo, B. *Rev. Sci. Instrum.* **2009**, *80* (12), 125105.